Magnetic Resonance in Medicine 45:684–691 (2001)

Signal-to-Noise Ratio and Absorbed Power as Functions of Main Magnetic Field Strength, and Definition of "90°" RF Pulse for the Head in the Birdcage Coil

Christopher M. Collins[1,3] and Michael B. Smith[1,2*]

Calculations of the RF magnetic (B_1) field as a function of frequency between 64 and 345 MHz were performed for a head model in an idealized birdcage coil. Absorbed power (P_{abs}) and SNR were calculated at each frequency with three different methods of defining excitation pulse amplitude: maintaining 90° flip angle at the coil center (center $\alpha = \pi/2$), maximizing FID amplitude (Max. A_{FID}), and maximizing total signal amplitude in a reconstructed image (Max. A_{image}). For center $\alpha = \pi/2$ and Max. A_{image}, SNR increases linearly with increasing field strength until 260 MHz, where it begins to increase at a greater rate. For these two methods, P_{abs} increases continually, but at a lower rate at higher field strengths. Above 215 MHz in MRI of the human head, the use of FID amplitude to set B_1 excitation pulses may result in apparent decreases in SNR and power requirements with increasing static field strength. Magn Reson Med 45:684–691, 2001. © 2001 Wiley-Liss, Inc.

Key words: calculations; SNR; power; MRI; high field

Predictions of trends in signal-to-noise ratio (SNR) and specific energy absorption rate (SAR) with increasing static magnetic field (B_0) strength based on MR theory, the principle of reciprocity, and analytical RF magnetic field (B_1) calculations have been shown to be reasonably accurate at frequencies up to 64 MHz in head- and body-sized samples (1,2). MRI experiments are currently performed at static magnetic field (B_0) strengths as high as 8.0 Tesla, where the frequency of the RF magnetic field (B_1) for imaging with ^{1}H is about 340 MHz. At these frequencies, significant interaction between the applied B_1 field and human tissues is expected. The effects of this interaction on SNR and the total absorbed power are complicated, and are dependent on the experiment being performed, RF coil type and performance, and even on the specific subject geometry and position in the coil (2,3).

In this study we performed calculations of SAR in the head, the total absorbed power (P_{abs}) in the head and shoulders, and SNR on an axial plane of the head at several B_1 frequencies between 64 and 345 MHz for an anatomically-accurate model in an idealized birdcage coil. The head position and orientation, and the coil behavior are kept constant so that B_1 frequency and definition of the excitation pulse are the only variables. Electrical properties of all tissues are set appropriately at each frequency. The excitation pulse amplitude is defined with three different methods at each frequency.

Since our interest was primarily in the effects of the high-frequency RF fields on the imaging experiment, we chose to ignore several factors that complicated both the calculation and interpretation of the results. We chose to consider signal from protons in water only, and to ignore T_1 and T_2 relaxation effects in this work. This simplifies the presentation of results, making them independent of TE and TR, but it also removes some realism from the simulation. We also neglected many other experimental effects, such as those of B_0 inhomogeneity, inevitable variation in sample and coil geometry, signal filtering, and signal amplifier integrity and performance (4). Thus, the findings concerning signal in the images, FID amplitude, and SNR presented here should be considered predictions of the types of phenomena that may be seen at high frequency due to behavior of the RF fields. Manifestation of these phenomena in experiment should not be expected to occur exactly as in these calculations.

METHODS

The finite difference time domain (FDTD) numerical method for electromagnetics was used to calculate all electrical and magnetic fields throughout a head model in an idealized birdcage coil. This method of calculation has previously been described in the literature (5,6). Here we present our methods for modeling the MR experiment with the FDTD method, and then relate the calculated results to the MR experiment.

Head Model

A model of the human head for use with the FDTD method was created by first segmenting 120 digital photographic images of axial slices through a male cadaver from the National Library of Medicine's Visible Human Project into 20 materials (18 tissues, one free space, and one metal dental filling), and then transforming these segmented images into a 3D grid of Yee cell cubes. One computer program was written to perform the transformation, and another was written to ensure the continuity of skin on the outer surface of the model. Segmentation was performed manually with reference to textbooks on anatomy and with assistance from two practicing radiologists. At each frequency, appropriate values from the literature for tissue mass density (7–10), water content by percent mass (11), and electrical permittivity and conductivity (12) were assigned to each tissue. Tissue mass density information was

[1]Department of Radiology, Pennsylvania State University College of Medicine, Hershey, Pennsylvania.

[2]Department of Cellular and Molecular Physiology, Pennsylvania State University College of Medicine, Hershey, Pennsylvania.

[3]Department of Bioengineering, University of Pennsylvania, Philadelphia, Pennsylvania.

*Correspondence to: Michael B. Smith, Center for NMR Research, NMR/MRI Building, Department of Radiology H066, Pennsylvania State University College of Medicine, 500 University Drive, Hershey, PA 17033.
E-mail: mbsmith@psu.edu

Received 22 March 2000; revised 2 November 2000; accepted 6 November 2000.

used in calculation of SAR, and water content was used to weight signal from different tissues differently in calculation of simulated images. Electrical permittivity and conductivity are necessary in the calculation of RF fields. The final mesh resolution is Δ_x, Δ_y, and Δ_z = 2, 2, and 2.5 mm, respectively, where Δ_x is in the model's left-right direction, Δ_y is in the model's anterior-posterior direction, and Δ_z is in the model's inferior-superior direction. A significant portion of the shoulders was included to extend the model well below the end of the coil and avoid problems at the boundary of the model experienced previously (13). Several slices through the model are shown in Fig. 1. Detailed description and diagrams of the model and tissue property assignments are available (14).

Coil Model and Field Solutions

The birdcage coil (12 legs, 30-cm diameter, 25-cm length) was modeled with perfectly-conducting material in the position of the legs and end rings, and with equal-amplitude voltage sources placed at the center of each leg and in the middle of each end ring segment. Legs were modeled as thin wires, while end rings were modeled with entire Yee cell cubes (6) of dimensions Δ_x, Δ_y, and Δ_z = 2, 2, and 2.5 mm, respectively. In the first field calculation, end-ring voltage sources were driven at a phase equal to the azimuthal angle with voltage sources on opposite end rings having opposite polarity, and leg voltage sources were driven at a phase equal to the azimuthal angle plus 90°. The result is a voltage distribution consistent with one possibility for a band-pass birdcage resonator in ideal quadrature resonance. The larger circularly-polarized component ($\hat{B}_1^+$) of this field was determined as

$$\hat{B}_1^+ = (\hat{B}_x^a + i\hat{B}_y^a) \div 2 \qquad [1a]$$

where $\hat{B}_x^a$ and $\hat{B}_y^a$ are the complex amplitudes of *x*- and *y*-oriented RF magnetic fields, respectively, as created by the coil driven as just described, where *i* is the imaginary unit, and where imaginary components are 90° out of phase with real ones. The circumflex is used to indicate a complex number. The complex amplitude (both magnitude and phase information) of the circularly-polarized component is necessary in the calculation of FID amplitude. In order to derive both the magnitude and phase of the circularly-polarized components of an elliptically-polarized field, both the magnitude and phase of its *x*- and *y*-oriented components must be considered. A second field calculation was performed with voltage sources driven

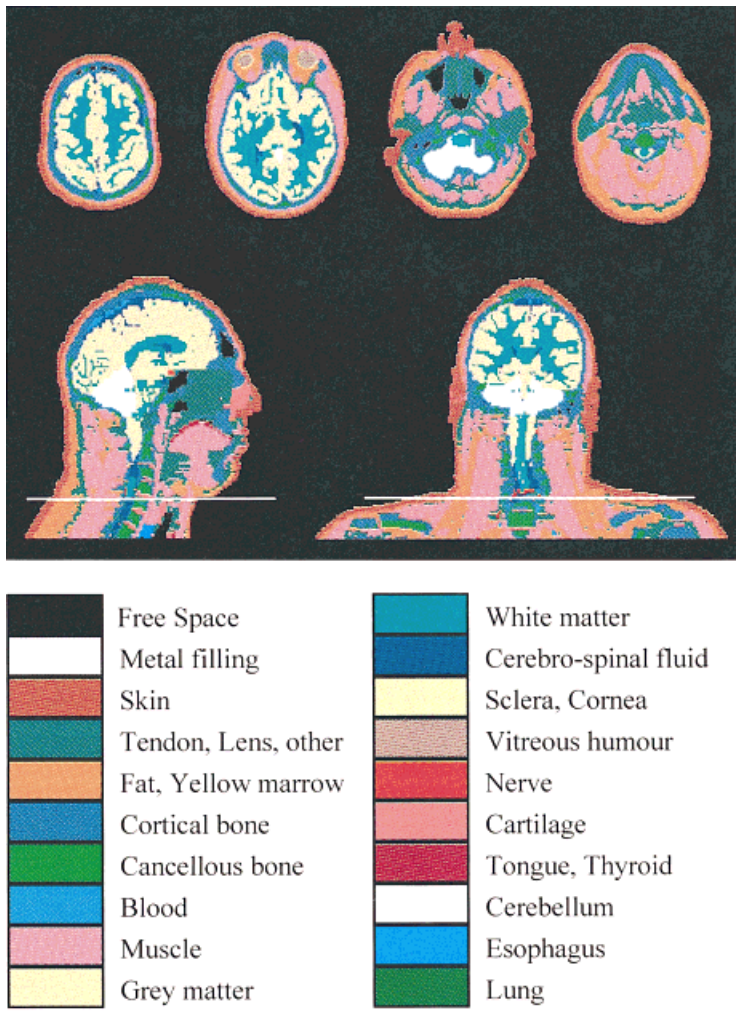

FIG. 1. Slices through a 3D head and shoulders model with Δ_x, Δ_y, and Δ_z = 2, 2, and 2.5 mm, respectively. Top: Axial slices through the head at 5-cm intervals. Bottom left: Sagittal slice through the middle of the model. Bottom right: Coronal slice chosen to show extent of shoulders. Only the region above (superior to) the white line is considered the "head" for SAR calculations.

with phases opposite those in the first case. The larger circularly-polarized component ($\hat{B}_1^+$) of this field was determined as

$$\hat{B}_1^- = (\hat{B}_x^b - i\hat{B}_y^b)^* \div 2 \qquad [1b]$$

where the superscript b indicates fields generated by this second configuration and the asterisk indicates the complex conjugate. It is possible to simulate actual coil resonance to some degree with the FDTD method (15,16). Since in an experiment every coil behaves differently, and since in this work we are interested more in the field interaction with the human head than in the exact behavior of any one coil, ideal coil approximations are more appropriate for this study. Calculations were performed at 64, 125, 175, 215, 260, 300, and 345 MHz (corresponding, roughly, to 1.5, 3, 4, 5, 6, 7, and 8 Tesla B_0 field strengths). All field solutions were set up and performed with the aid of commercially available software (XFDTD; Remcom, Inc., State College, PA) on an IBM RS/6000 model 550 computer with 1.0 GB of RAM.

Normalization for Three Different Excitation Pulses

After the field calculation, all fields and SAR values were normalized as if to produce a rectangular excitation pulse with a duration (τ) of 3 msec on the axial plane at the center of the coil (hereafter referred to as the "imaging plane"). The field magnitude during this pulse was defined in three ways at each frequency.

In the first method (center $\alpha = \pi/2$) a flip angle (α) of 90° was induced at a point at the center of the coil. Thus a normalization factor, V, is determined so that $V/|\hat{B}_1^+| = \alpha/\gamma\tau = 1.957\mu T$ at the coil center where $|\hat{B}_1^+|$ is the absolute value of $\hat{B}_1^+$ and γ is the gyromagnetic ratio of ^1H.

In the second method (Max. A_{FID}) the amplitude of the FID (with no phase- or frequency-encoding) was maximized. In order to calculate the FID amplitude, it is necessary to sum the contribution of all voxels considering both the magnitude and phase of the induced signal. With increasing B_1 frequency the electromagnetic wavelength in tissue decreases. Consequently, the spatial variation in the phase of $\hat{B}_x$ and $\hat{B}_y$ in Eq. [1] increases, and so does the spatial variation in phase of $\hat{B}_1^+$ and $\hat{B}_1^-$. The signal induced in the coil by nuclei at different locations may interfere destructively in a given FID. The FID amplitude was calculated as (17):

$$A_{FID} \propto \left|\sum_N W_n \sin(V|\hat{B}_{1n}^+|\gamma\tau) e^{i\beta_{1n}^+} (\hat{B}_{1n}^-)^*\right| \qquad [2]$$

where β_{1n}^+ is the phase of $\hat{B}_{1n}^+$ ($\beta_{1n}^+ = \text{atan}[\text{Imag}(\hat{B}_{1n}^+)/\text{Real}(\hat{B}_{1n}^+)]$) in the nth voxel, $\hat{B}_{1n}^+$ is $\hat{B}_1^+$ of the nth voxel, W_n is the water content (by percent mass) of the nth voxel, and V is a normalization factor. The summation is performed over all voxels on the imaging plane, where one voxel is represented by each Yee cell. The summation is maximized by varying V. Only the first local maximum (closest to $V = 0$) is considered.

In the third method (Max. A_{image}) the amplitude of the total signal contributing to a reconstructed gradient echo image is maximized. While in a single FID with no frequency- or phase-encoding (as in Eq. [2]) the phase of signal from different locations may result in signal cancellation, in the reconstructed image (where the signal from each voxel has been separated according to position) only the magnitude of the signal in each voxel and the sensitivity of the coil to the location of each voxel are important. A_{image} was calculated as

$$A_{image} \propto \sum_N \|W_n \sin(V|\hat{B}_{1n}^+|\gamma\tau)|(\hat{B}_{1n}^-)^*\|. \qquad [3]$$

The summation is performed over all voxels on the imaging plane, where one voxel is represented by each Yee cell. The summation is maximized by varying V. Only the first local maximum (closest to $V = 0$) is considered.

Since the voltage sources provided 1 volt in the initial calculation, the normalization factor, V, necessary to achieve these three criteria will be equal to the voltage value (in volts) in the coil voltage sources associated with the final field patterns.

Signal Intensity Distributions

To estimate what a gradient-echo (GE) image might look like at a given frequency, we calculate the signal intensity from each voxel as proportional to the absolute values of the sine of the flip angle ($\sin(\alpha) = \sin(V|B_{1n}^+|\gamma\tau)$) of the spins in the voxel, the sensitivity of the receiving coil (the complex conjugate of $\hat{B}_1^-$) to spins in the voxel, and the water content (W) in the voxel.

SNR Calculation

The methods used here for calculating SNR are very similar to those of Edelstein et al. (1), who had success at lower frequencies in describing the trend in "intrinsic" SNR with frequency using only analytical models of RF field behavior. For the entire imaging plane,

$$\text{SNR} \propto f^2 \frac{\sum_N \|W_n \sin(V|\hat{B}_{1n}^+|\gamma\tau)|(\hat{B}_{1n}^-)^*\|}{\sqrt{P_{abs}}} \qquad [4]$$

where the summation is performed over all voxels in the imaging plane and P_{abs}, the total absorbed power in the entire model, is calculated as

$$P_{abs} = \frac{1}{2}\sum_N (\sigma_{xn}E_{xn}^2 + \sigma_{yn}E_{yn}^2 + \sigma_{zn}E_{zn}^2)\Delta_x\Delta_y\Delta_z \qquad [5]$$

where E and σ are the electric field magnitude and material conductivity, respectively, and the summation is performed over all voxels in the model. As with $\hat{B}_1^+$, the values of E and P_{abs} correspond to the field magnitudes where $V = 1$.

SAR Calculation

For comparison with standard limits on SAR levels in the head, only the region above the white line in Fig. 1 was

evaluated in finding maximum 1-cm^3 SAR (SAR_{1cc}) and head-average SAR (SAR_{ave}). For calculation of SAR_{1cc}, the average SAR values of the 100 cells in every 1-cm^3 region were calculated and the maximum of these averages was found. SAR_{ave} is calculated as the average SAR in all voxels. Since the highest SAR levels are in soft tissue, where material density is very nearly 1 g/cm^3, it is appropriate to use the maximum SAR in any 1 cm^3 for comparing with limits in any 1 g of tissue. SAR at every location in the model is calculated as

$$\mathrm{SAR} = \frac{\sigma_x}{2\rho_x} E_x^2 + \frac{\sigma_y}{2\rho_y} E_y^2 + \frac{\sigma_z}{2\rho_z} E_z^2 \qquad [6]$$

where ρ is the local material density.

RESULTS AND DISCUSSION

B_1 and SAR Distributions

Figure 2 contains shaded plots of $V|\mathbf{B}_1|$ and V^2SAR at 64 MHz. Plots on three orthogonal planes are given so that the 3D field and SAR patterns can be seen. The $|\mathbf{B}_1|$ distribution is seen to be very homogeneous throughout the coil at this frequency, and most of the power is absorbed towards the outer surface of the head, as is expected from field calculations with approximations appropriate for low frequencies, where it is not as important to consider the effect of the sample on the B_1 field (18).

Figure 3 shows the distribution of VB_1^+ ($B_1^+ = |\hat{B}_1^+|$), of the signal intensity (SI) of a gradient-echo image, and of V^2SAR on the imaging plane at four selected frequencies when the center $\alpha = \pi/2$ for a 3-msec rectangular pulse. As frequency increases, the B_1^+ distribution becomes more complicated and the SAR distribution is no longer concentrated towards the outside of the head. This demonstrates that low-frequency approximations will be less valid at the high MR frequencies used today. Because flip angle is directly proportional to VB_1^+, it is also apparent from Fig. 3 that at frequencies as high as 345 MHz it is impossible to define a true "90°" pulse on an entire plane through the head. At high frequencies, flip angle will vary widely with position.

P_{abs} and SNR

In calculating P_{abs} we neglected the RF energy absorbed by the nuclei as they are excited to their respective higher energy states, seen classically as a greater flip angle. At 1.0T the difference in energy between 1 cc of protons in water at $\alpha = 0°$ and $\alpha = 90°$ is about 3.0 nJ (19). This increases proportionally to $|\mathbf{B}_0|^2$. Based on the water content values in our model, a 1-cm-thick axial slab around the imaging plane will contain about 200 cc of water. Thus, exciting all the ^{1}H nuclei in water in this slab to 90° will require about 1.35 μJ at 1.5T and about 38.4 μJ at 8.0T. This is less than 0.1% of the energy absorbed in the head by conduction currents induced by the coil ($V^2P_{abs}\tau$ = 4.08 mJ at 1.5T and 43.8 mJ at 8T for center $\alpha = \pi/2$ and τ = 3 msec).

In Table 1 the normalization factors V (also equal to the driving voltage in volts) necessary to produce the excitation desired with each of the three methods at all seven frequencies are given, along with the resulting total absorbed power in the model (V^2P_{abs}), the relative SNR, and V^2SAR values in the head for comparing with FDA limits. The following paragraphs include discussion of all of these values, including the dip in SNR for Max. A_{FID} seen at 260 MHz.

In addition to the numerical values in Table 1, Line plots of V^2P_{abs} and SNR as functions of frequency for the three excitation methods are given in Figs. 4 and 5, respectively. Using an excitation pulse that produces a center $\alpha = \pi/2$ or that maximizes A_{image} will result in a continual increase in V^2P_{abs} and in SNR. Values of V^2P_{abs} increase at a decreasing rate at frequencies above about 215 MHz for center α =

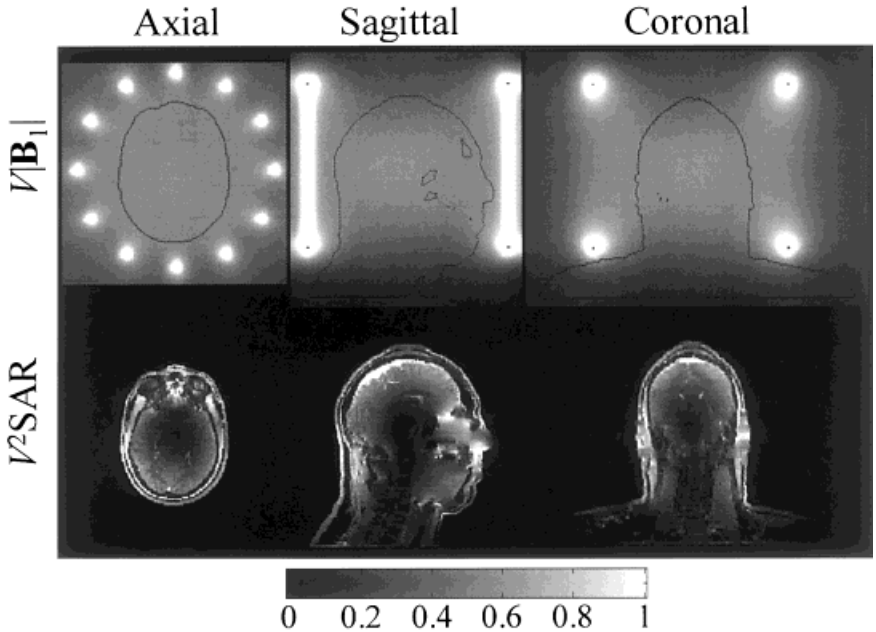

FIG. 2. Distributions of $V|\mathbf{B}_1|$ (top) and V^2SAR (bottom) for head in idealized birdcage coil at 64 MHz for 3-msec rectangular pulse to achieve a 90° flip at center (center $\alpha = \pi/2$). Gray scale is expressed in terms of a fraction of maximum scale value. Maximum scale value is 5μT for $V|\mathbf{B}_1|$, and 0.5334 W/kg (three times head average value) for V^2SAR. Values above scale maximum are expressed as the same (white) intensity as the scale maximum.

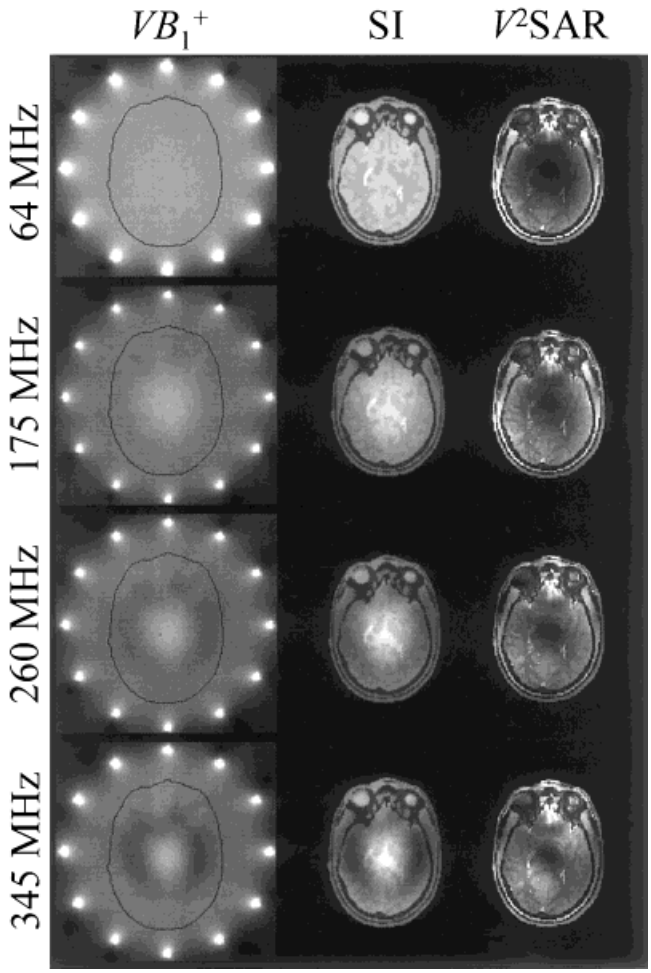

FIG. 3. Distributions of VB_1^+ (left), relative detected signal intensity during a gradient-echo sequence (SI, center), and V^2SAR (right) for the imaging plane (axial plane at center of coil) through the head in an ideal birdcage coil at several frequencies for center $\alpha = \pi/2$. Gray scale as in Fig. 2, with a scale maximum of 5μT for VB_1^+, 1.0 for relative detected signal intensity, and three times V^2SAR_{ave} (Table 1) for V^2SAR.

$\pi/2$. This demonstrates that the low-frequency approximations, which predict an increase of V^2P_{abs} proportional to f^2 (1), are less valid at high frequencies. This predicted trend of decreasing slope in absorbed power at high frequencies for a constant flip angle at one point is consistent with previous calculations that considered Maxwell's equations in their entirety for simple geometries with near-physiologic parameters (20). An understanding of why this deviation from low-frequency estimates occurs can be gained by looking at the B_1 flux through a plane and considering Faraday's law. Figure 6 shows the magnitude and phase of the B_1 flux through the center sagittal plane in the head model at 345 MHz. At 345 MHz the electromagnetic wavelength in brain tissue is about 12 cm. Thus, at these frequencies it can be useful, conceptually, to think of the B_1 field as magnetic waves originating at the coil elements, traveling towards the center of the head, and interfering constructively when they meet there (21). At very high frequencies used today in MR of the head with volume coils, the B_1 field will have opposite phases at different locations on a given plane through the head (Fig. 6). This results in a cancellation of net flux through the plane and thus, by Faraday's law:

$$\left| \oint_l \mathbf{E} \cdot d\vec{l} \right| = \left| -i2\pi f \int_s B \cdot d\vec{s} \right| \qquad [7]$$

lower induced electric field magnitudes around the perimeter of the head than would be predicted with estimates assuming a field with homogeneous phase. This results in lower conduction current densities and lower absorbed power than predicted assuming homogeneous fields. Notice that if a homogeneous magnetic field B and material characteristics are assumed at all frequencies f, the induced electric fields will be proportional to frequency. Absorbed power, which is proportional to $|E|^2$, will then be proportional to f^2. As indicated in Fig. 6, this is clearly not the case at high frequencies in the human head.

In agreement with theory and experiment at frequencies up to 64 MHz (1,2), SNR increases at a rate roughly proportional to f at frequencies below 260 MHz when using an excitation pulse that produces center $\alpha = \pi/2$ or that maximizes A_{image}. Between about 175 MHz and 260 MHz the slope of this line can be seen to decrease slightly because we are calculating SNR for an entire plane, which has a decreasing homogeneity of flip angles with increasing frequency. Above 260 MHz the rate of increase of SNR with frequency increases. This corresponds with a decrease in the slope of V^2P_{abs}, which is expected to have an increasing slope in low-frequency estimates. This predicted trend of increasing slope in SNR at high frequencies for a constant flip angle at a point is consistent with previous calculations that considered Maxwell's equations in their entirety for simpler samples with near-physiologic parameters (20,22). In these previous calculations the slope increases more continually because the SNR at one point is considered, so there is no decreasing homogeneity in a volume of interest.

It is clear in Figs. 4 and 5 that using the amplitude of the FID (A_{FID}) to determine the excitation pulse in the head at frequencies above 215 MHz can lead to unexpected, misleading results. At any given time during signal acquisition, voltages induced in the receiving coil by different nuclei may oppose each other. At low frequencies this ordinarily does not occur unless the nuclei become dephased by gradient fields or an otherwise inhomogeneous static field. At very high frequencies, where wavelength effects are apparent in the B_1 field distribution, this can occur regardless of static and gradient field behavior.

Figure 7 shows A_{FID} and A_{image} as functions of the center α for a 3-msec duration (τ) excitation pulse at each frequency. This is useful in examining the behavior of A_{FID} relative to A_{image} with increasing driving voltage (proportional to center α) at all frequencies. The cancellation of signal amplitude resulting from wavelength effects on phase are especially apparent in the low amplitude of the first A_{FID} peak at 260 MHz (Fig. 7), as opposed to at lower

Table 1
Normalization Factor V, Total Absorbed Power (V^2P_{abs}), SNR, Average SAR in the Head (V^2SAR_{ave}), and Maximum SAR in 1 cm^3 in the Head (V^2SAR_{1cc}) for Three Different Excitation Methods at Seven Different Frequencies

f (MHz)	Excitation method	V	V^2P_{abs} (W)	SNR	V^2SAR_{ave} (W/kg)	V^2SAR_{1cc} (W/kg)
64	Center $\alpha = \pi/2$	14.2	1.36	30.3	0.178	0.875
	Max. A_{FID}	14.7	1.46	30.3	0.190	0.937
	Max. A_{image}	14.7	1.46	30.3	0.190	0.937
125	Center $\alpha = \pi/2$	19.7	4.42	54.0	0.570	2.99
	Max. A_{FID}	22.9	5.97	55.3	0.770	4.04
	Max. A_{image}	22.9	5.97	55.3	0.770	4.04
175	Center $\alpha = \pi/2$	21.7	6.96	71.1	0.878	4.81
	Max. A_{FID}	27.7	11.4	75.2	1.44	7.87
	Max. A_{image}	27.6	11.3	75.2	1.43	7.82
215	Center $\alpha = \pi/2$	24.0	9.22	82.0	1.10	5.15
	Max. A_{FID}	32.9	17.2	88.1	2.07	9.68
	Max. A_{image}	31.8	16.2	88.3	1.93	9.04
260	Center $\alpha = \pi/2$	29.5	12.3	94.4	1.33	6.47
	Max. A_{FID}	22.8	7.35	84.1	0.794	3.86
	Max. A_{image}	38.6	21.0	99.8	2.28	11.1
300	Center $\alpha = \pi/2$	31.2	13.8	119.	1.45	6.72
	Max. A_{FID}	34.4	16.8	124.	1.76	8.16
	Max. A_{image}	44.1	27.5	132.	2.90	13.4
345	Center $\alpha = \pi/2$	29.9	14.6	151.	1.57	8.15
	Max. A_{FID}	36.2	21.3	164.	2.30	11.9
	Max. A_{image}	42.4	29.4	168.	3.16	16.4

frequencies. At 64 MHz, where B_1 is very homogeneous, there is good correlation in the size and position (along the x-axis) between A_{FID} and A_{image}. Since α at the center point is proportional to driving voltage for a given pulse type and duration, this indicates that at low frequencies A_{FID} is a useful indicator of A_{image}, and can thus be used effectively to determine what excitation will result in the most signal on a reconstructed image. At 125 and 175 MHz (Fig. 7) the amplitude of A_{FID} drops below that of A_{image}, but the position of the first peak along the x-axis still correlates well with that of A_{image}, so A_{FID} is still a viable indicator of A_{image} in determining an excitation pulse. However, at 260 MHz and above it is apparent that the result of signal cancellation is causing both the amplitude and position of the first peak in A_{FID} to decrease. Thus, maximizing A_{FID} to determine the excitation pulse can result in a lower SNR over the plane than could be achieved (Fig. 5), and a lower P_{abs} than at lower frequencies using the same method (Fig. 4).

For this particular imaging plane in this particular head and coil model, a maximum cancellation of A_{FID} will occur around 260 MHz, resulting in a sharp dip in SNR and P_{abs} when A_{FID} is maximized. One other set of calculations indicates that such situations of maximum signal

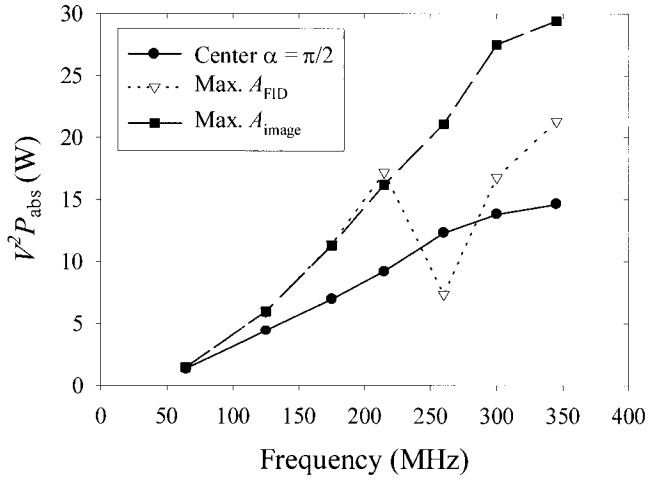

FIG. 4. Absorbed power with increasing frequency for three different excitation methods: a 3-msec rectangular pulse is used to either make the center flip angle 90° (Center $\alpha = \pi/2$), maximize the unencoded FID amplitude from the imaging plane (Max. A_{FID}), or maximize the integrated image amplitude (Max. A_{image}).

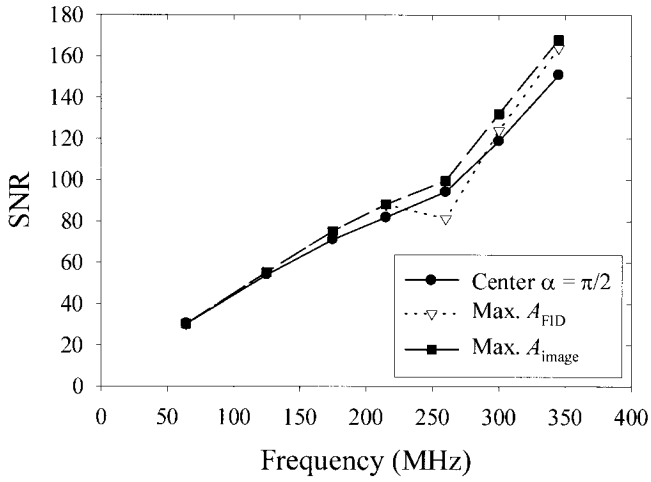

FIG. 5. SNR with increasing frequency for three different excitation methods. Here the entire imaging plane is treated as a single volume for SNR calculation, so B_1 inhomogeneity is a factor.

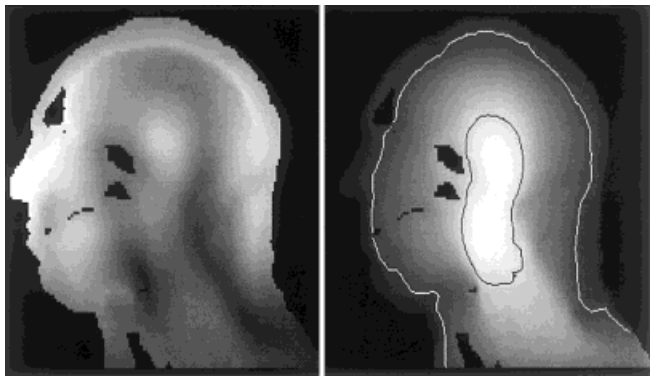

FIG. 6. Shaded plots of the magnitude (left) and phase (right) of the *x*-oriented (normal to the sagittal plane) component of the VB_1 field (V for $\alpha_c = 90°$) at 345 MHz. The scale maximum for the magnitude plot is 2.5 mT (gray scale in a fraction of the scale maximum, as in Fig. 2). The range of phase values in the plane shown encompasses 262°. The black and white contours are at phase values 180° apart.

cancellation may be observable (23), resulting in dips in SNR with increasing frequency (field strength) for a sphere with properties of a weakly conductive dielectric material. Because this dip is due to opposing phases in the plane caused by wavelength effects, we would expect it to occur at higher frequencies on smaller cross-sections (and in a smaller head) and at lower frequencies on larger cross-sections.

At any given frequency the amount of power absorbed varies much more with the excitation method (Fig. 4) than does SNR on the entire plane (Fig. 5). Given this and the difficulty of setting the excitation pulse by the integrated image intensity experimentally, it may be desirable to set the excitation pulse according to the flip angle at one location of interest. If the excitation pulse is set to maximize signal from the center point, much less power will be required than if the excitation pulse is set to maximize the overall image amplitude, and the overall SNR will not be significantly different.

SAR and Regulatory Limits

It is possible to use the results here to calculate SAR values for specific experiments with other pulses, pulse sequences, and repetition times (24). As previously published, it is expected that many standard imaging sequences can be performed at frequencies as high as 345 MHz without exceeding current established limits on SAR (25). In fact, all of the SAR levels here are lower than our previously published levels (24) for a simpler head model when the excitation pulse was determined by making the average α in the head on the imaging plane equal to 90°. The excitation case here with mean flip angles closest to 90° is where A_{image} is maximized (Max. A_{image}). Mean flip angles in this case are 89°, 87°, and 84° at 64, 125, and 175 MHz, respectively. At all other frequencies (215–345 MHz), the mean flip angle was 82°. Correcting for mean flip angle, Max. A_{image} has 20–30% lower SAR_{ave} than our previous calculations and 14–50% lower SAR_{1cc}. Since the model used here is much more anatomically accurate, this suggests that model accuracy is an important factor in estimating SAR levels. Still, compared to measurements in homogeneous phantoms, these methods with either model should give acceptable estimates of SAR levels.

Consistent with our previous calculations (24), local (1 g) SAR limits will be exceeded before average SAR limits are. This reinforces the importance of having good methods for predicting local SAR levels. In these calculations the maximum local SAR level occurred in the soft tissue anterior to the cheekbone at 64, 260, and 300 MHz; in the masticator space at 125, 175, and 215 MHz; and in the upper lip just below the base of the nose at 345 MHz.

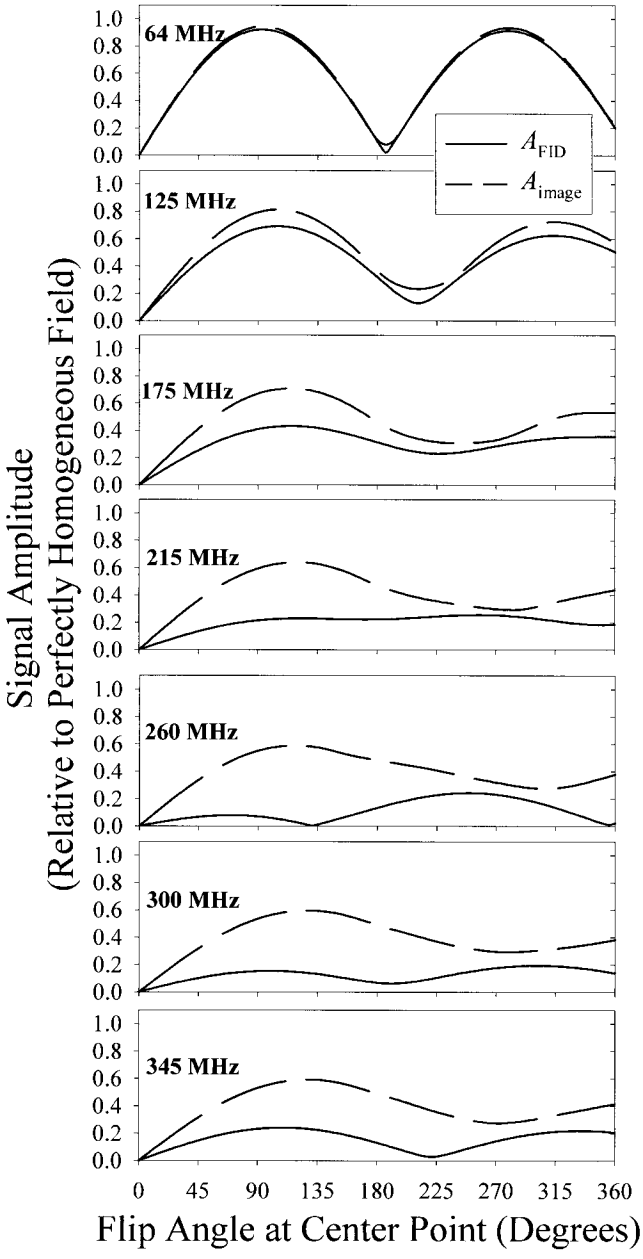

FIG. 7. A_{image} and A_{FID} with increasing center flip angle at several different frequencies. Here values are expressed as a fraction of the value at the given frequency for a perfectly homogeneous B_1 field. Since both A_{FID} and A_{image} are calculated for the entire imaging plane, B_1 field inhomogeneity affects their values.

However, a slightly different configuration (head geometry and position, coil geometry, etc.) or definition of local SAR region (shape and size) would likely result in maxima at different locations.

Limitations of Methods

These results are useful in indicating trends related to RF field behavior at high B_1 frequencies, but the actual values observed in experiment will depend on the actual coil, sample, and imaging protocol used in experiment. For example, if a smaller head or smaller cross-section through the head (through a superior plane) were used, wavelength effects might not affect A_{FID} until a higher frequency, and P_{abs} will likely be significantly less. Also, experimental SNR values are dependent on many factors not considered here, such as static field homogeneity (susceptibility effects and line broadening), T_1 and T_2 of tissues, TE and TR, slice thickness, and receiver bandwidth (2). For fatty tissues, water content may not be an accurate estimate of proton density for some sequences with a low TE, since protons in lipid ordinarily have a significant signal in these sequences. In future calculations it may be useful to consider some of these factors.

CONCLUSIONS

Full-Maxwell calculations for an anatomically-accurate head in an idealized birdcage coil indicate a fairly linear increase of SNR (over an axial planar slice through the head) with increasing frequency for frequencies up to 260 MHz when the excitation pulse is designed either to achieve $\alpha = 90°$ at the coil center or to produce maximum total signal on the reconstructed image. This agrees well with low-frequency theoretical expectations and experimental results. These calculations also predict a slight increase in the slope of SNR with frequency above 260 MHz. In imaging of the human head at frequencies above 215 MHz, the amplitude of a single FID should not be used to accurately predict the total signal amplitude in a reconstructed image or to predict the "flip angle" of a given pulse, as flip angle depends on position in the sample at these frequencies.

Calculations of absorbed power and SAR suggest that these entities will not increase with B_1 frequency nearly as fast as expected with low-frequency approximations. In fact, the slope of absorbed power with increasing frequency will decrease with increasing frequency, rather than increase. These calculations, in combination with methods for calculating SAR for specific sequences, indicate that a number of experiments could be performed at frequencies as high as 345 MHz in the head with a quadrature volume coil without exceeding current limits on SAR.

ACKNOWLEDGMENTS

We have benefited greatly from enlightening discussions and correspondence with Dr. David I. Hoult, including rigorous proofs of the necessary equations for calculating detected signal. We are also grateful to Belinda G. Collins, M.D., Ph.D., and Timothy J. Mosher, M.D., for their expert advice in segmenting images for the production of the head model used here.

REFERENCES

1. Edelstein WA, Glover GH, Hardy CJ, Redington RW. The intrinsic signal-to-noise ratio in NMR imaging. Magn Reson Med 1986;3:604–618.
2. Hoult DI, Chen C-N, Sank VJ. The field dependence of NMR imaging: ii. arguments concerning an optimal field strength. Magn Reson Med 1986;3:730–746.
3. Wen H, Denison TJ, Singerman RW, Balaban RS. The intrinsic signal-to-noise ratio in human cardiac imaging at 1.5, 3, and 4 T. J Magn Reson 1997;125:65–71.
4. Chen C-N, Sank VJ, Cohen SM, Hoult DI. The field assessment of NMR imaging: I. Laboratory assessment of signal-to-noise ratio and power deposition. Magn Reson Med 1986;3:722–729.
5. Yee KS. Numerical solution of initial boundary value problems involving Maxwell's equations in isotropic media. IEEE Trans Ant Propag 1966;14:302–307.
6. Kunz KS, Luebbers RJ. The finite difference time domain method for electromagnetics. Boca Raton: CRC Press; 1993.
7. Wlodzimierz E, Gos T. Density of trunk tissues of young and medium age people. J Biomech 1990;23:945–947.
8. Huang HK, Wu SC. The evaluation of mass densities of the human body in vivo from CT scans. Comput Biol Med 1976;6:337–343.
9. Cho ZH, Tsai CM, Wilson G. Study of contrast and modulation mechanisms in x-ray/photon transverse axial transmission tomography. Phys Med Biol 1975;20:879–889.
10. Clauser CE, McConville JT, Young JW. Weight, volume, and center of mass of segments of the human body. Aerospace medical research laboratory, Wright-Patterson Air Force Base, Ohio: AMRL-TR-69-70; 1969.
11. Duck FA. Physical properties of tissue. London: Academic Press; 1993.
12. Gabriel C. Compilation of the dielectric properties of body tissues at RF and microwave frequencies. Air Force materiel command, Brooks Air Force Base, Texas: AL/OE-TR-1996-0037; 1996.
13. Jin JM, Chen J, Chew WC, Gan H, Magin RL, Dimbylow PJ. Computation of electromagnetic fields for high-frequency magnetic resonance imaging applications. Phys Med Biol 1996;41:2719–2738.
14. Collins CM. Calculations of RF magnetic fields and SAR experienced by the human body during MRI. Doctoral dissertation, University of Pennsylvania, 1999.
15. Junge S, Haeberlen U. 3D simulations of B and E fields in RF resonators by CONCEPT and MAFIA. In: Proceedings of the 6th Annual Meeting of ISMRM, Sydney, Australia, 1999. p 2042.
16. Ibrahim TS, Yu Y, Lee R, Baertlein BA, Kangarlu A, Robitaille P. Finite difference time domain simulations for high-field MRI. In: Proceedings of the 6th Annual Meeting of ISMRM, Sydney, Australia, 1999. p 652.
17. Hoult DI. The principle of reciprocity in signal strength calculations—a mathematical guide. Concepts Magn Reson 2000;4:173–187.
18. Bottomley PA, Andrew ER. RF magnetic field penetration, phase shift and power dissipation in biological tissue: implications for NMR imaging. Phys Med Biol 1978;23:630–643.
19. Abragam A. Principles of nuclear magnetism. Oxford: Oxford University Press; 1961. p 71–72.
20. Keltner JR, Carlson JW, Roos MS, Wong STS, Wong TL, Buddinger TF. Electromagnetic fields of surface coil *in vivo* NMR at high frequencies. Magn Reson Med 1991;22:467–480.
21. Collins CM, Smith MB. Toward understanding power requirements in high-field imaging of the head: instantaneous B_1 flux and Faraday's law. In: Proceedings of the 8th Annual Meeting of ISMRM, Denver, 2000. p 647.
22. Ocali O, Atalar E. Ultimate intrinsic signal-to-noise ratio in MRI. Magn Reson Med 1998;39:462–473.
23. Hoult DI. The sensitivity and power deposition of the high field imaging experiment. J Magn Reson Imaging 2000;12:46–67.
24. Collins CM, Li S, Smith MB. SAR and B_1 field distributions in a heterogeneous human head model within a birdcage coil. Magn Reson Med 1998;40:847–856.
25. International Electrotechnical Commission. Medical electrical equipment, part 2: particular requirements for the safety of magnetic resonance equipment for medical diagnosis. IEC 601-2-33; 1995.